Manipulation of Antiskyrmion Phase in $Mn_{2+x}Ni_{1-x}Ga$ Tetragonal Heusler System

Subir Sen,[1] K. Somesh,[2] R. Nath,[2] and Ajaya K. Nayak[1,*]

[1] *School of Physical Sciences, National Institute of Science Education and Research, HBNI, Jatni 752050, India*
[2] *School of Physics, Indian Institute of Science Education and Research Thiruvananthapuram, Kerala 695551, India*

(Received 19 November 2021; revised 23 February 2022; accepted 1 April 2022; published 21 April 2022)

The inhomogeneous magnetization distribution in antiskyrmions helps in nullifying the unwanted skyrmion Hall effect generally found in the current driven motion of skyrmions. At present, the observation of room-temperature antiskyrmion phase is limited to only a very few materials. Here, we present the evidence of a tunable antiskyrmion phase in the D_{2d}-symmetry-based tetragonal Heusler system $Mn_{2+x}Ni_{1-x}Ga$. With the help of dc magnetization, ac susceptibility, and topological Hall effect measurements, we demonstrate that the potential antiskyrmion phase can be tuned over a wide compositional range with magnetic ordering temperature of above 600 K. In addition, we find the existence of multiple topological phase transitions for a certain Mn/Ni ratio where the magnetic anisotropy attains its maxima. Our micromagnetic simulations suggest that the transition from antiskyrmionium and antiskyrmion pockets to the conventional antiskyrmion phase at the optimal value of magnetic anisotropy might be responsible for the observed multiple topological transitions in the present materials. The expected small size of antiskyrmions in the present low magnetic-moment-based ferrimagnetic system gives a great advantage over other skyrmion and antiskyrmion hosting materials for their potential application in racetrack-based memory devices.

DOI: 10.1103/PhysRevApplied.17.044040

I. INTRODUCTION

Skyrmions, which are proposed to be the building blocks in the next-generation racetrack-based memory devices owing to their inherent topological stable structure, can be interpreted as swirling kinds of noncoplanar localized spin textures with size ranging from few nanometers to micrometer [1]. The topological nature of the skyrmions can be firmly determined by the skyrmion number and/or topological charge $N_{sk} = 1/4\pi \int\int \mathbf{m} \cdot (\partial\mathbf{m}/\partial x \times \partial\mathbf{m}/\partial y)\, dxdy$, where, $\mathbf{m}$ is the unit vector along the local magnetization. For skyrmions, the topological charge can take integer values (± 1). In certain noncentrosymmetric magnetic systems, e.g., B20 compounds [1–7], β-Mn structured Co-Zn-Mn [8], and GaV_4S_8 [9], the presence of competing Dzyaloshinkii-Moriya (DM) interaction and Heisenberg exchange sets the helical spin modulation as the ground state. In general, application of magnetic field perpendicular or with some angle to the helical propagation direction stabilizes Bloch or Néel-type skyrmions in these systems [1–12].

The nature of the skyrmions is solely determined by the crystal symmetry and hence the DM vector. In the case of the above discussed materials, the isotropic nature of the DM vectors, i.e., $D_x = D_y$, where D_x and D_y are the DM vectors along x and y directions, respectively, sets the homogeneous chirality of spin rotation in all direction. In contrast, an anisotropic DM vector ($D_x = -D_y$) in the case of D_{2d}-symmetry-based inverse tetragonal Heusler materials has led to a special class of skyrmions, named *antiskyrmions*, as recently observed in Mn-Pt-Pd-Sn system [13–18]. The anisotropic nature of the DM interaction gives rise to a change in the spin chirality in every $\pi/2$ cycle, forcing the spin distribution to undergo Bloch to Néel-type arrangement in every $\pi/4$ rotation. The special symmetry of these materials ensures the propagation of the helical phase along the (100) or (010) directions. Hence, the antiskyrmion lattice can be effectively stabilized by the application of magnetic field along (001) direction [10,13,16,17]. The skyrmions and antiskyrmion lattices can also be stabilized with the application of oblique magnetic fields, where the stability largely depends on the easy-axis anisotropy of the system [10]. In this framework, it is often found that the application of magnetic field with some angle to the high-symmetry -4 axis in the D_{2d}-symmetric materials distorts the crystal-symmetry-governed spin texture, e.g., shifting of the antiskyrmion core without changing the direction of the antiskyrmion

*ajaya@niser.ac.in

 © 2022 American Physical Society

axis [10] and transformation of antiskyrmion to skyrmion via trivial bubble [16,17]. However, this type of deformation of the antiskyrmion can be minimized when the magnetic field is applied near to the (001) direction [13].

The inhomogeneous type of magnetization distribution in antiskyrmions makes a difference in their current driven dynamics. It has been shown that skyrmions deviate from their straight-line motion under the electric field due to the well-known *skyrmion Hall effect*, which is an unwanted quantity in device applications [19,20]. In contrast, the anisotropic nature of spin distribution stabilized by asymmetric DM interaction in antiskyrmions effectively contributes to their current driven motion. In a normal situation of current flow, the antiskyrmion is expected to display the conventional topologocal Hall effect and skyrmion Hall effect as it carries a topological charge of -1, which is opposite to that of skyrmion. The antiskyrmion Hall effect can be tuned to zero when the current is passed at a critical direction [21]. Therefore, it is useful to stabilize and manipulate antiskyrmion phase in suitable materials. In this direction, the D_{2d}-symmetry-based inverse tetragonal Heusler materials are ideal candidates to host the antiskyrmion lattice [13]. In a recent study, the signature of room-temperature antiskyrmion phase has been reported in D_{2d}-symmetric compound Mn_2NiGa [22]. In addition, Mn_2NiGa exhibits a very high Curie temperature (T_C) of about 650 K and the presence of perpendicular magnetic anisotropy makes it an ideal candidate for spintronic applications. In addition, the antiskyrmion size in Mn_2NiGa is expected to be in the order of 10 nm. For any future application of the antiskyrmions, it is worthwhile to study their stabilization in extended magnetic field and temperature range, along with greater tunability of its size. Such control can be achieved by the appropriate choice of exchange coupling, DM interaction, and magneto-crystalline anisotropy in the system. The exchange coupling strength can be manipulated by modifying the electron filling and the bond lengths, while the DM interaction and magnetocrystalline anisotropy depend on the strength of spin-orbit coupling (SOC).

In the present work, we systematically study the effect of the aforementioned parameters on the potential antiskyrmion phase in $Mn_{2+x}Ni_{1-x}Ga$ ($x = 0.0$ to 0.28). By doing so, we demonstrate the evidence of multiple topological phase transitions for a certain compositional range. Finally, our experimental results are well supported by micromagnetic simulation.

II. METHODS

A series of polycrystalline samples of composition $Mn_{2+x}Ni_{1-x}Ga$ ($x = 0.10$, 0.13, 0.16, 0.20, 0.25, and 0.28) are prepared by arc-melting ultrahigh pure constituent elements in argon atmosphere. As prepared ingots are sealed in quartz tubes under argon atmosphere and annealed for 7 days at 1073 K. Room-temperature powder x-ray diffraction (XRD) measurements are performed using a Rigaku SmartLab x-ray diffractometer with a Cu-K_α source. The compositional homogeneity of the samples are studied by field-emission scanning electron microscope (FESEM) equipped with energy-dispersive x ray (EDX).

The low-temperature dc magnetization (M) measurements below $T = 400$ K are performed using a superconducting quantum interference device vibrating sample magnetometer (SQUID VSM, Quantum Design) and the high-temperature magnetization studies are performed using a VSM attached to a Physical Property Measurement System (PPMS, Quantum Design). The ac susceptibility measurements are carried out using PPMS in an ac field, $H_{ac} = 10$ Oe and frequency $f = 7777$ Hz in linear-persistent mode. Magnetotransport data of Hall bar samples are recorded at different temperatures by utilizing the PPMS. The micromagnetic simulation is carried out using the software package Object Oriented Micromagnetic Framework (OOMMF).

III. RESULTS AND DISCUSSION

The room-temperature XRD patterns for the $Mn_{2+x}Ni_{1-x}Ga$ samples are plotted in Fig. 1(a). The XRD pattern systematically evolves from a mixed tetragonal and cubic phases with space group I-4m2 and F-43m, respectively, for $x = 0$ to a pure tetragonal phase for $x \geq 0.10$. Since the XRD measurements are performed on the disc-shaped samples, only certain peaks are observed due to the preferred orientation of the corresponding grains in the polycrystalline samples. The unit cell corresponding to the inverse tetragonal structure (space group I-4m2) for the present system with extra Mn atoms partially replacing Ni is shown in the inset of Fig. 1(a). In addition to the XRD data, we also confirm the phase and compositional purity of these samples using the EDX facility in FESEM (see the Supplemental Material [23]).

In order to study the magnetic properties of our well-characterized samples, a series of temperature-dependent magnetization measurements [$M(T)$] are carried out in the temperature range of 2 to 400 K under field-cooling (FC) and field-heating (FH) modes, as depicted in Fig. 1(b). The presence of a pronounced thermal hysteresis between the FC and FH $M(T)$ curves in the case of the parent Mn_2NiGa sample signifies the structural phase transition from the low-temperature tetragonal to the high-temperature cubic phase. The transition shifts to a temperature of about 350 K for $x = 0.1$, as marked by an arrow. However, no such transition anomaly is found in the $M(T)$ curves for samples with higher Mn concentration ($x > 0.10$). We also carry out high-temperature $M(T)$ measurements up to 750 K for some selected $Mn_{2+x}Ni_{1-x}Ga$ samples, as shown in the inset of Fig. 1(b). Interestingly, no transitionlike feature

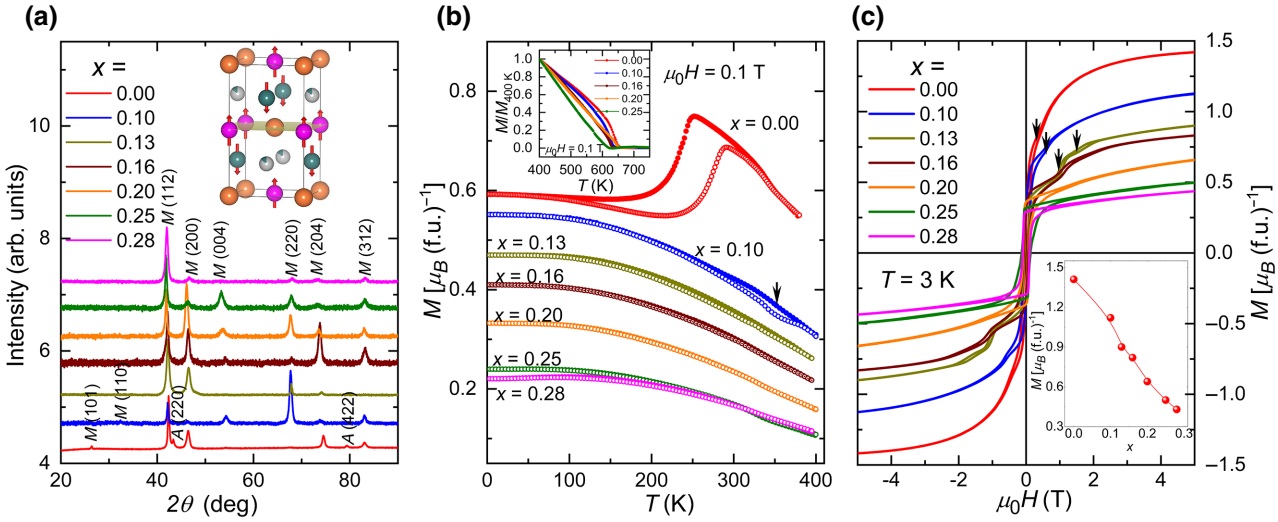

FIG. 1. (a) Room-temperature x-ray diffraction data for $Mn_{2+x}Ni_{1-x}Ga$ ($x = 0.0, 0.10, 0.13, 0.16, 0.20, 0.25$, and 0.28) samples. The peaks for $x = 0.0$ and 0.28 are indexed, where A and M correspond to austenite and martensite phases, respectively. The inset shows the tetragonal unit cell of $Mn_{2+x}Ni_{1-x}Ga$ system, where Mn1, Mn2, Ni, and Ga atoms are represented by magenta, dark cyan, gray, and orange solid spheres, respectively. The solid arrows indicate the direction of magnetic moment on each site. (b) Temperature-dependent magnetization, $M(T)$, curves for $Mn_{2+x}Ni_{1-x}Ga$ measured at $H = 0.1$ T in field-cooled (FC) and field-heating (FH) modes, as shown by solid and open circles, respectively. The inset represents $M(T)$ data for different samples at higher temperatures ($T > 400$ K). (c) Field dependence of magnetization, $M(H)$, for $Mn_{2+x}Ni_{1-x}Ga$ taken at $T = 3$ K. The inset shows the compositional dependence of the saturation magnetization.

is observed in the high-temperature data above 400 K, signifying that all samples with $x \geq 0.13$ crystallize only in the tetragonal structure up to the T_C.

The field-dependent isothermal magnetization measurement [$M(H)$] performed at $T = 3$ K is presented in Fig. 1(c). The parent compound Mn_2NiGa exhibits a small metamagneticlike transition (marked by arrows) around 0.45 T. This transition becomes more prominent for $x = 0.1$ around 0.60 T. Interestingly, the sample with $x = 0.13$ displays two clear metamagnetic-type transitions: one at about 1 T and the second one at 1.8 T (marked by arrows). Similar types of transitionlike features are also found for $x = 0.16$. However, the sample with $x = 0.2$ displays only a single transition, as found for the parent Mn_2NiGa compound. Finally, no transition is observed in the $M(H)$ isotherm for $x = 0.25$ and 0.28. It can also be seen from the $M(H)$ curves that the saturation magnetization monotonically decreases from 1.4 μ_B (f.u.)$^{-1}$ for Mn_2NiGa to about 0.43 μ_B (f.u.)$^{-1}$ for $Mn_{2.28}Ni_{0.72}Ga$, just by increasing the Mn concentrations [inset of Fig. 1(c)]. It is well known that in the case of Mn_2YZ system [24], where Y is a transition metal and Z is the main group element, the Mn atoms occupy two different lattice sites. The Mn atoms sitting in the Mn-Y plane with a tetrahedral surrounding carry a lower magnetic moment than the Mn atom in the Mn-Z plane with octahedral environment. In addition, the Mn moments at two different lattice planes are arranged antiferromagnetically to each other. Since the extra Mn atoms in the present system occupy the Mn-Y plane, it results in a net decrease in the magnetic moment in the system.

The finding of multiple field-induced transitions in the $M(H)$ measurements for $x = 0.13$ and 0.16, motivated us to probe the magnetotransport properties of these samples. Figure 2(a) shows the field-dependent Hall resistivity ρ_{xy} for $x = 0.13$ measured at room temperature. The ρ_{xy} data display a small dip kind of behavior at a field of about 0.3 T marked by the down arrow, followed by two more transitions at higher fields: at around 1 T (marked by the star) and 2 T (marked by the up arrow). We also find a substantial hysteretic behavior between the field-increasing and decreasing ρ_{xy} curves around the transition region. To further investigate the observed anomaly in the ρ_{xy} data, the room-temperature $M(H)$ loop and its first derivative (dM/dH) are plotted in Figs. 2(b) and 2(c), respectively. Distinct anomalies in both the $M(H)$ and dM/dH curves clearly indicate the existence of a low field transition around 0.3 T as marked by down arrows, along with two other transitions at higher fields. Furthermore, we also perform ac susceptibility measurements, where the real part of the ac susceptibility, $\chi'(H)$, curve exhibits a distinct peak around 1 T, accompanied by two additional transitions at 0.3 and 2 T as seen in Fig. 2(d). The sharp transition around 1 T is also clearly seen in the imaginary part of the ac susceptibility [$\chi''(H)$] data, whereas the small humplike features around 0.3 and 2 T are not visible clearly due to instrumental resolution limit [Fig. 2(e)]. All these measurements corroborate our findings of field-induced anomalies

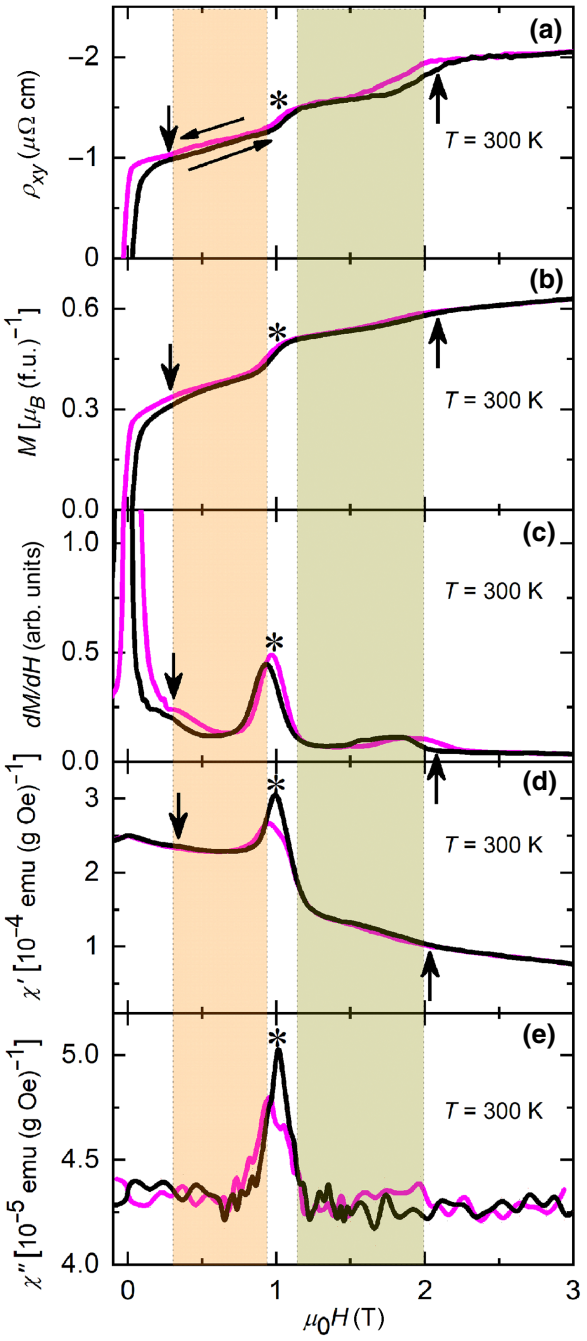

FIG. 2. Field dependence of (a) Hall resistivity ρ_{xy}, (b) magnetization loop, (c) first derivative of the magnetization (dM/dH), (d) the real part of ac susceptibility as a function of field, $\chi'(H)$, and (e) the imaginary part of ac susceptibility as a function of field, $\chi''(H)$, measured at 300 K for the $x = 0.13$ sample. The magenta and black lines in all plots represent field-decreasing and field-increasing paths, respectively. The presence of field-induced transitions are marked by down arrows at low field (approximately equal to 0.3 T), stars at intermediate fields (approximately equal to 1 T), and up arrows at high fields (approximately equal to 2 T). The region between the low and intermediate field transitions is shown by orange shading, whereas the region between the intermediate and high fields is marked by the dark yellow shading.

in the ρ_{xy} data. Based on these field-induced transitions, we could identify two primary phase regimes: the region between the low and intermediate field transitions, marked by the orange shading and the region between the intermediate and high field transitions, highlighted by the dark yellow shading.

The observation of multiple transitions in the Hall resistivity and magnetic measurements in some of the $Mn_{2+x}Ni_{1-x}Ga$ samples motivates us to throw more light onto the possible existence of topological magnetic phase. For this purpose, we plot the experimental Hall resistivity data along with the calculated Hall resistivity ($\rho^A + \rho^N$) for all the $Mn_{2+x}Ni_{1-x}Ga$ samples in Fig. 3. It is well known that the Hall resistivity in ferro- and ferrimagnetic materials with additional topological Hall component can be expressed as the sum of three Hall components, ρ^N, ρ^A, and ρ^T, where, ρ^N represents the normal Hall resistivity that varies linearly with external magnetic field, ρ^A stands for the anomalous Hall resistivity, which generally scales with the magnetization of the sample, and ρ^T refers to the extra component of Hall resistivity, named as topological Hall resistivity, which is neither proportional to the external magnetic field nor to the magnetization of the samples. The ρ^T often emerges due to the presence of noncoplanar spin textures including skyrmions and antiskyrmions. Hence, the experimental Hall resistivity can be written as $\rho_{xy} = R_0H + R_SM + \rho^T$, where R_0 is the normal Hall coefficient and R_S is the anomalous Hall coefficient that is related to the longitudinal resistivity (ρ_{xx}). In our case, ρ^A mainly originates from the intrinsic mechanism, whereas R_S is proportional to ρ_{xx}^2 (see the Supplemental Material [23]). The extrinsic contributions to the Hall resistivity, such as skew-scattering and side-jump mechanisms, are neglected for the present system as the longitudinal Hall conductivity falls under the moderate conductivity regime ($10^4 < \sigma_{xx}$ [$(\Omega$ cm$)^{-1}$] $< 10^6$) [25]. Hence, we can rewrite the total Hall resistivity as $\rho_{xy} = R_0H + b\rho_{xx}^2M + \rho^T$. The application of very high magnetic fields in general destroys the topological objects as the sample transforms into the field polarized state, resulting in a vanishing ρ^T. It can also be seen that the anomaly in the ρ_{xy} measurements present only in the small to moderate field regime (≤ 2 T). Therefore, at very high fields the total Hall resistivity can be written as $\rho_{xy} = R_0H + b\rho_{xx}^2M$ or $\rho_{xy}/H = R_0 + b\rho_{xx}^2M/H$. To extract ρ^T, first the R_0 and b are calculated at the high-field regime from the straight-line fitting of the ρ_{xy}/H vs ρ_{xx}^2M/H plot. Using the R_0 and b values, we calculate ρ_{xy} for field regime $H = \pm 5$ T to ∓ 5 T, which are shown as red lines on the top of the experimental Hall resistivity data in Fig. 3.

It can be clearly seen that the calculated Hall resistivity matches well with the experimental data in the whole field regime, except the fields where anomalies are seen in the ρ_{xy} data for $x = 0$ to 0.2. This suggests the existence of some additional topological phases in these samples.

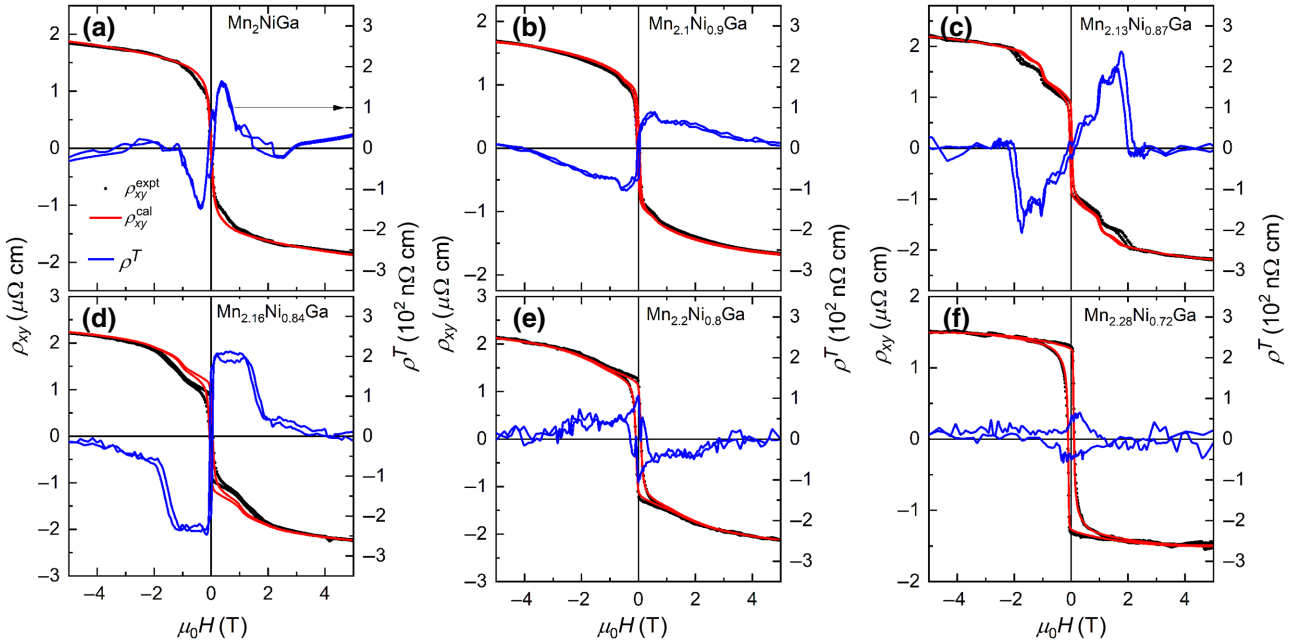

FIG. 3. (a)–(f) Field-dependent experimental Hall resistivity ρ_{xy} (left y axes, scattered solid circles) measured at $T = 300$ K for $Mn_{2+x}Ni_{1-x}Ga$ samples. The fitted lines to the experimental ρ_{xy} data represent the calculated Hall resistivity taking into account the anomalous and the normal Hall resistivity ($\rho^A + \rho^N$) (red lines). The extracted topological Hall resistivity (ρ^T, right y axes) is shown as blue lines.

The experimental and the calculated Hall resistivity curves fully match in the whole field range for $x = 0.28$, where no anomaly is seen in the ρ_{xy} curves. To further access the topological states in the system, we subtract the calculated anomalous and normal Hall components from the total Hall resistivity. The extracted ρ^T is plotted as blue lines (right y axes) in Fig. 3. As can be seen, ρ^T changes systematically from one peaklike behavior for $x = 0$ to a two-step feature in $x = 0.1 - 0.16$. Interestingly, the ρ^T again changes to a single peaklike behavior with change in sign for $x = 0.2$. Finally, no topological Hall effect (THE) is found for $x = 0.28$.

To further probe the possible existence of the topological phase transition, we perform ac susceptibility measurements on the $Mn_{2+x}Ni_{1-x}Ga$ samples as depicted in Fig. 4. It is noteworthy to mention here that the ac susceptibility measurements are widely used as a characterization tool to identify skyrmions and antiskyrmions in several systems [8,26–29]. From the $\chi'(H)$ curves it is apparent that samples with $x = 0$, 0.13, 0.16, and 0.2 show a very sharp peak at about 1 T ($\triangledown$) with an additional hump kind of behavior around 2 T for $x = 0.13$, 0.16, and 0.2 [marked by $\bigoplus$ in Figs. 4(a)–4(d)]. As discussed earlier, $x = 0.16$ also exhibits a small transition kind of anomaly at a very low field indicated by $\star$. The transition at 1 T can also be seen clearly in the $\chi''(H)$ data, marked by arrows in Figs. 4(f)–4(h). However, the transition at high fields cannot be seen in the $\chi''(H)$ plots, as its magnitude falls in the instrumental resolution limit. Of note, all the transitions are accompanied by hysteresis in the field-increasing and decreasing paths, signifying the first-order nature of the transitions [30]. It can be noted here that a similar kind of transition anomaly was recently observed in the ac susceptibility measurements in the case of the Heusler tetragonal antiskyrmion hosting Mn-Pt-Pd-Sn system [15]. Hence, our ac susceptibility measurements point towards the presence of antiskyrmion phase in the present system. The absence of any transition in both $\chi'(H)$ and $\chi''(H)$ curves for $x = 0.28$, which also does not show any THE, further vindicate our findings.

In order to further investigate the evolution of possible antiskyrmion phase in our samples, the role of various energy parameters such as exchange constant (J), DM constant (D), and magnetocrystalline anisotropy (K) needs to be understood, as the size and stability of the antiskyrmion phase largely depend on these parameters. It has been reported [31] that the size of the skyrmion R, can be expressed as $R = \pi D\sqrt{A/(16AK^2 - \pi^2 D^2 K)}$, where A is the exchange stiffness constant that proportionally varies with the exchange constant J. In our case, the exchange stiffness remains almost constant as the magnetic ordering temperature for all the samples falls between 600 and 650 K. In the previous study, it has been found that the magnetic anisotropy plays a decisive role along with the inhomogeneous DM interaction in the formation of

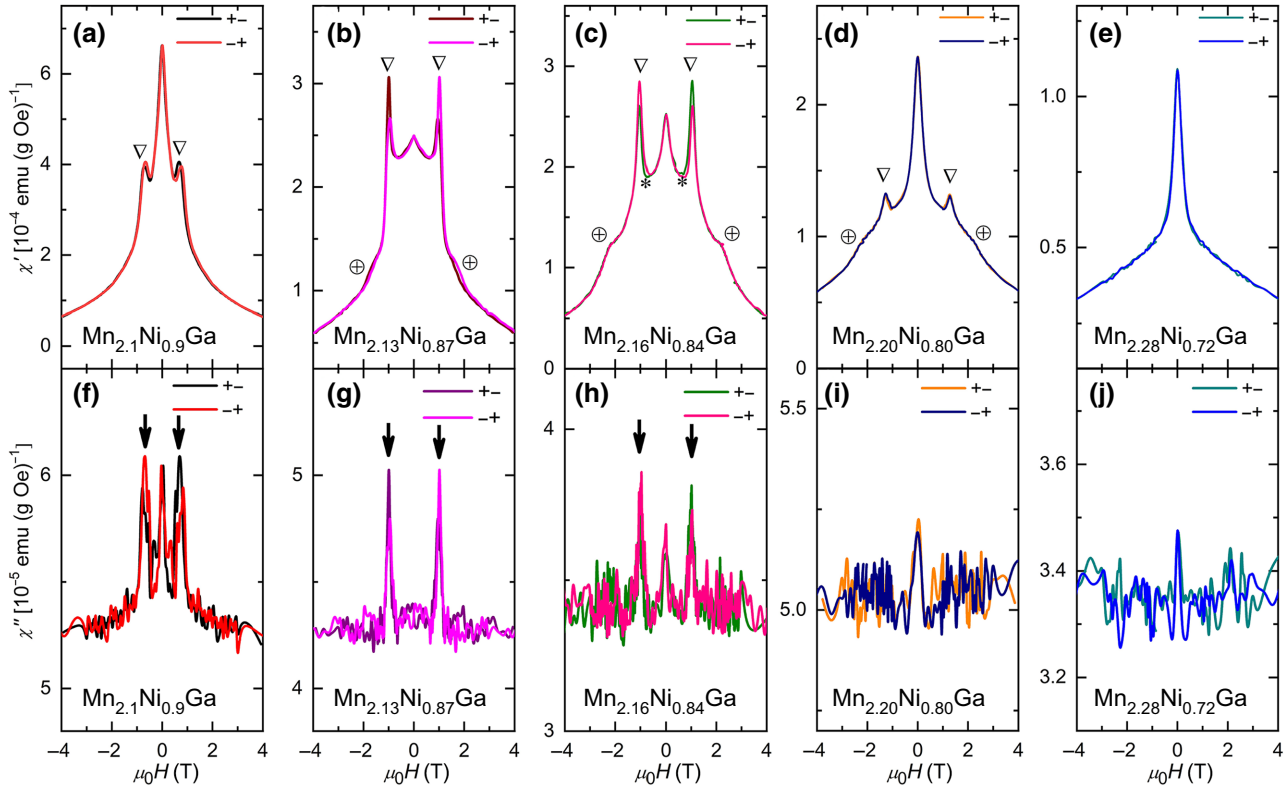

FIG. 4. (a)–(e) Room-temperature real part of ac susceptibility as a function of magnetic field, $\chi'(H)$ for $Mn_{2+x}Ni_{1-x}Ga$ samples. The notations "+−" and "−+" indicate the field sweep from +5 to −5 T and −5 to +5 T, respectively. The symbols ▽, ⨁, and ⋆ mark the transitions in $\chi'(H)$ curves. (f)–(j) Field-dependent imaginary part of ac susceptibility, $\chi''(H)$ plots at $T = 300$ K. Transitions in the curves are marked by arrows.

antiskyrmion phase in the case of Mn_2NiGa [22]. To extract the uniaxial magnetocrystalline anisotropy in the present samples, we follow the law of approach to saturation (LAS) [23,32]. According to the LAS method, the magnetization M of highly anisotropic ferromagnetic samples in the region with $M \geq 0.95M_s$ can be expressed as $M = M_s(1 - a_2/H^2)$, where M_s is the spontaneous magnetization and a_2 is a constant for a given system at a fixed temperature. In the case of uniaxial anisotropic polycrystalline systems, $a_2 = 4K_{\text{eff}}^2/15M_s^2$, where K_{eff} is the effective magnetocrystalline anisotropy constant. It is to be noted here that the above relation between a_2 and M_s is formulated by averaging the contribution of all grains oriented in different directions with respect to the magnetic field in the polycrystalline sample [32]. Now, if we consider the demagnetization effect, then the internal magnetic field in the sample (H') can be given by $H' = H - NdM$, where d is the mass density and N is the demagnetization factor that lies in between 0 and 1 [33–35]. Since we measure the magnetization by applying the magnetic field perpendicular to the long axis of rectangular cubiod-shaped samples, N in this configuration is found to be about 0.45–0.65 [33–35]. The inset of Fig. 5 shows the M versus $1/H'^2$ (solid symbols) plot for the $Mn_{2.13}Ni_{0.87}Ga$ sample. In order to evaluate the uniaxial magnetocrystalline anisotropy of the samples, we fit the experimental data using the LAS relation $M = M_s(1 - a_2/H'^2)$, as shown in the inset of Fig. 5. From the straight-line fitting, the values of M_s and a_2 are obtained as 163 769.612 ±125.224 A m^{-1} and 1.843 ± 0.022 T^2, respectively. Using these fitting parameters K_{eff} is calculated as 4.30 (±0.10) ×10^5 J m^{-3} for $Mn_{2.13}Ni_{0.87}Ga$. A similar procedure is followed to calculate the effective uniaxial magnetocrystalline anisotropy constant for other samples.

The variation of K_{eff} with composition for the $Mn_{2+x}Ni_{1-x}Ga$ samples is plotted in Fig. 5 (open square symbols). As can be seen, K_{eff} first increases monotonically with x and achieves a maxima for $x = 0.13$, before decreasing for the higher x samples. To compare the effect of anisotropy with the observed THE, the compositional variation of maximum ρ^T is also plotted in Fig. 5 (open circles). As can be seen, ρ^T exhibits a similar kind of peak behavior as that of K_{eff}. It is noteworthy to mention here that the ρ^T is related to the size of antiskyrmions (a_{sk}) by the relation $\rho^T \approx (h/e)PR_0/{a_{\text{sk}}}^2$, where R_0 is the normal Hall coefficient and P is the spin polarization of the

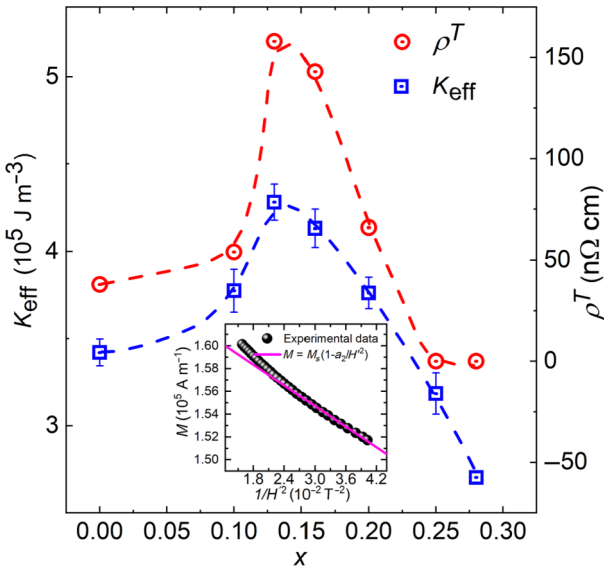

FIG. 5. Variation of magnetic uniaxial anisotropy constant (K_{eff}) and maximum value of topological Hall resistivity (ρ^T) for $Mn_{2+x}Ni_{1-x}Ga$ samples taken at $T = 3$ K. The symbols represent the data points, whereas the dotted lines act as a guide to eye. The inset shows experimental (solid circles) and the fitted magnetization curve (solid line) using the LAS relation $M = M_s(1 - a_2/H'^2)$ for $Mn_{2.13}Ni_{0.87}Ga$ when the magnetization $M \geq 0.95M_s$.

conduction electrons [36]. With the above relation, the antiskyrmion size a_{sk} for $x = 0.13$ and 0.16 is estimated to be less than 10 nm. Therefore, it is evident that the increase in K_{eff} plays a substantial role in the reduction of antiskyrmion size for $x = 0.13$ and 0.16 with maximum THE.

The finding of multiple transitions in the Hall resistivity and magnetization measurements for $x = 0.13$, which also exhibits the highest anisotropy, prompted us to carry out micromagnetic simulation to understand its origin. The simulation is carried out with the help of public domain software package OOMMF [37], added with the DMI extension module [38]. Here, we take a thin film with dimensions of $1000 \times 1000 \times 5$ nm^3 with a cell size of $5 \times 5 \times 5$ nm^3. We start the simulation from a randomly magnetized state and then the magnetic state is relaxed in the presence of a magnetic field of 0.55 T with different values of anisotropies fixing the saturation magnetization to $M_S = 1.65 \times 10^5$ A m^{-1}, the DM interaction constant to $D = 6$ mJ m^{-2}, and the exchange stiffness to $A = 3 \times 10^{-11}$ J m^{-1}. Figure 6 shows the evolution of spin textures with different values of anisotropies K. A mixed state of different spin textures, e.g., antiskyrmions with different helicity, antiskyrmioniums, and stripe domains, coexist for the lower anisotropy constants ranging from 1×10^5 J m^{-3} to 4×10^5 J m^{-3}. Interestingly, the presence of topological magnetic textures, such as antiskyrmions, antiskyrmioniums [as shown inside the white dashed boxes in Fig. 6(f)], and antiskyrmion pockets with opposite helicity [as shown inside the black dashed boxes in Fig. 6(f)] are found for $K = 5 \times 10^5$ J m^{-3}. Further increase in $K = 6 \times 10^5$ J m^{-3} mostly stabilizes pure antiskyrmion phase as shown in Figs. 6(g) and 6(h). These simulated results suggest that the magnetic anisotropy greatly affect the nature of spin textures in our system.

The observation of multiple transitions in the Hall measurements can be understood from our simulated magnetic textures presented in Fig. 7 along with the field variation of ρ^T. Here, the micromagnetic states represent the typical field evolution of the system with saturation magnetization $M_S = 1.65 \times 10^5$ A m^{-1}, $D = 6$ mJ m^{-2}, $A = 3 \times 10^{-11}$ J m^{-1}, and $K = 5 \times 10^5$ J m^{-3} (the effective anisotropy for $x = 0.13$). A possible correlation of all the simulated magnetic states at different magnetic fields with the field-dependent experimental topological Hall resistivity for $x = 0.13$ are presented in Fig. 7. Different field regions in the field evolution of ρ^T curves and the corresponding simulated magnetic spin states are denoted as R-1, R-2, R-3, and R-4. The following assessments can be made from Fig. 7. (1) For H_z = 0.3 T, a mixed magnetic state consisting of strip domains, antiskyrmions, antiskyrmion pockets with opposite helicity, and antiskyrmioniums is observed. It can be mentioned here that antiskyrmioniums consist of a zero topological charge, whereas the antiskyrmion pockets in the present case show opposite topological charge to that of the antiskyrmions. The small value of ρ^T in R-1 is due to the net topological charge coming from the antiskyrmions. (2) By further increasing the field to $H_z = 0.55$ T, as indicated by R-2, the stripe domain states disappear completely and predominantly a mixture of all topological magnetic states comprising of antiskyrmions, antiskyrmioniums, and the antiskyrmion pockets with opposite helicity are found. A small increase in ρ^T from R-1 to R-2 can be attributed to the creation of a larger number of antiskyrmions from the stripe domain state. (3) A sharp kind of transition can be noticed between R-2 and R-3. As can be seen from the simulated pattern at $H_z = 1.00$ T, all the antiskyrmioniums and the antiskyrmion pockets with opposite helicity, disappear in R-3, instead a dense arrangement of the regular antiskyrmions is found. This results in the observation of a sudden rise of ρ^T in the R-3 region, as all the antiskyrmionium with zero topological charge and antiskyrmion pockets with opposite helicity are now converted into regular antiskyrmions. (4) The field-polarized simulated state, represented by R-4, appears for H_z = 3.0 T. In this case, all the antiskyrmions annihilate into the field-polarized state giving rise to the zero value of ρ^T in region R-4.

The large THE of over 200 nΩ cm in the present system points towards the existence of very small

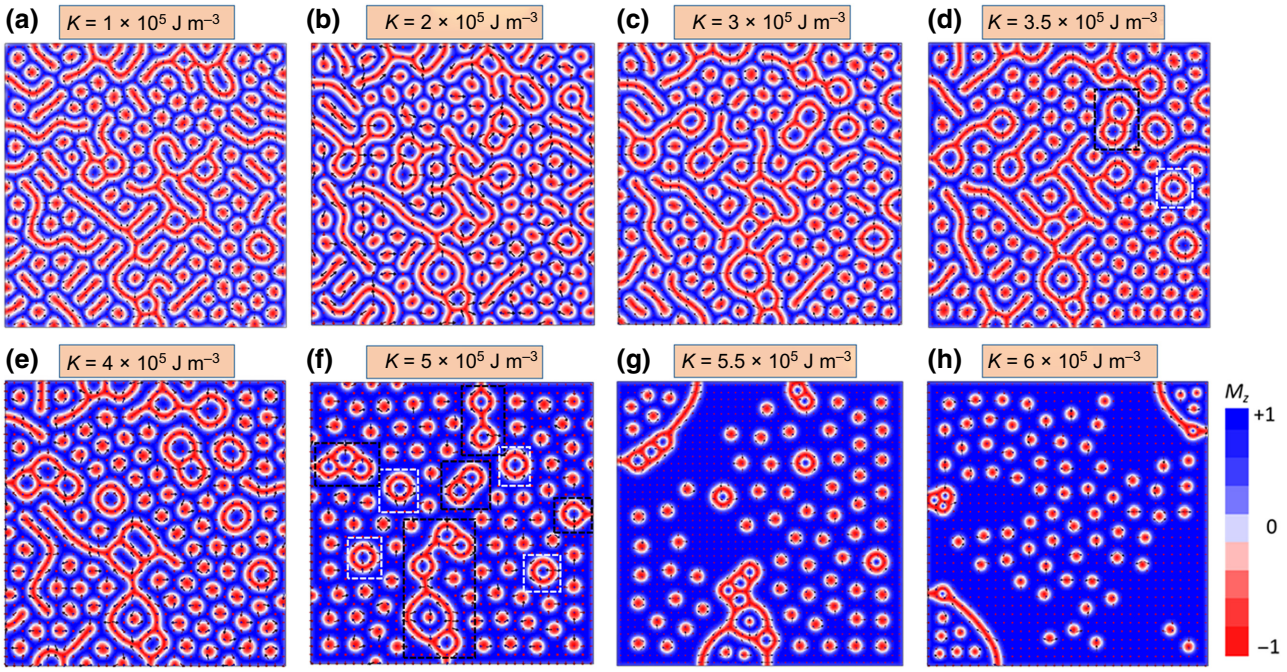

FIG. 6. Simulated spin textures showing the evolution of magnetic states with changing anisotropy. The simulation is carried out using the experimental saturation magnetic moment for $x = 0.13$, $M_S = 1.65 \times 10^5$ A m^{-1}, the DMI constant $D = 6$ mJ m^{-2}, and the exchange stiffness $A = 3 \times 10^{-11}$ J m^{-1}. A magnetic field of 0.55 T is applied for all the simulated textures. In (f) the antiskyrmioniums and antiskyrmion pockets are marked inside the white dashed boxes and black dashed boxes, respectively.

antiskyrmions of size less than 10 nm. It may be noted here that in the present polycrystalline samples, the measured THE originates only from the grains where c axis is aligned within 15–20° with respect to the applied magnetic field. Hence, the actual THE and antiskyrmion size in the present system could be much larger or smaller than the observed values. The small size of the antiskyrmions also restricts us to directly visualize them using Lorentz transmission electron microscopy. It is worthwhile to mention here that there are only few materials known to exhibit skyrmions of size <10 nm and in most of the cases, they exist at very low temperatures [7,39–43]. A very low-temperature skyrmion phase along with a narrow range of temperature stabilities in these materials are major shortcomings for room-temperature applications. In this prospect, the present Mn-Ni-Ga based tetragonal materials show the potential to host very small antiskyrmions (<10 nm) over a wide temperature range including the room temperature. Another aspect of the present system is that it shows a very small magnetic moment of less than 1 μ_B (f.u.)$^{-1}$. It has been observed that the antiskyrmions in highly magnetic samples can be easily transformed into skyrmions through the trivial bubble under the application of the very small in-plane magnetic field [16,17]. In such cases, the advantages of antiskyrmions over skyrmions regarding the skyrmion Hall effect are diluted by these topological phase transformation. Therefore, the present low magnetic-moment-based $Mn_{2+x}Ni_{1-x}Ga$ materials possess a high probability to host robust antiskyrmion phase unperturbed by the in-plane magnetic field and/or dipole field.

In a certain range of composition for the present system, the presence of various topological states with different topological charges is evident from the multiple topological transitions in different experimental data. Based on our micromagnetic simulation, these topological transitions are attributed to the possible presence of antiskyrmions along with antiskyrmioniums and antiskyrmion pockets. It is to be noted here that the finding of a similar kind of skyrmionium as well as skyrmion pockets has also been demonstrated recently in the skyrmion hosting FeGe thin plates [44]. The possibility of coexistence of the antiskyrmion and antiskyrmionium, which can be encoded as "1" and "0" data bits, respectively, makes the system more attractive for future spintronic applications. However, we are unable to directly visualize the proposed multiple topological states in our samples due to their small size. In future, other measurement techniques, e.g., small angle neutron scattering and resonant soft x-ray scattering can be utilized for their direct observation.

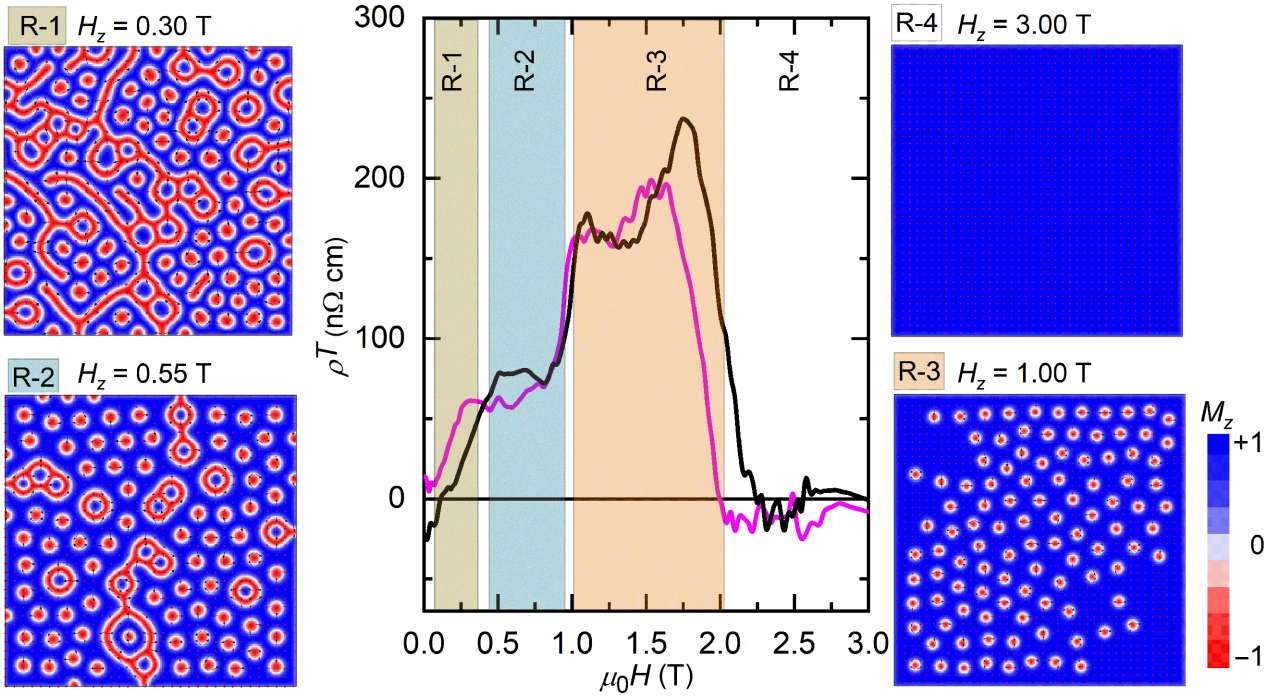

FIG. 7. Topological Hall resistivity along with field-dependent simulated spin textures for $x = 0.13$. The simulation is performed at different magnetic fields with $M_S = 1.65 \times 10^5$ A m^{-1}, $D = 6$ mJ m^{-2}, $A = 3 \times 10^{-11}$ J m^{-1}, and $K = 5 \times 10^5$ J m^{-3}. Different field regions in the ρ^T data and corresponding simulated magnetic textures are marked as R-1, R-2, R-3, and R-4.

IV. CONCLUSION

In conclusion, we carry out a detailed magnetic and Hall effect measurements to demonstrate the presence of potential antiskyrmion phase in the tetragonal Heusler materials $Mn_{2+x}Ni_{1-x}Ga$. Unlike the parent Mn_2NiGa, the antiskyrmion hosting tetragonal phase in the present case can be stabilized up to the magnetic ordering temperature of about 600 K. We show the existence of multiple topological phase transitions for a certain compositional range in the field evolution of topological Hall effect data as well as field-dependent ac susceptibility measurements. Our micromagnetic simulation suggests that the magnetic anisotropy of the system greatly contribute towards the stabilization of multiple topological states, possibly, antiskyrmionium and antiskyrmion pockets. Finally, the expected small size ($\lesssim$10 nm) of antiskyrmions at room temperature in the present system is extremely useful for the high-density memory applications.

ACKNOWLEDGMENTS

This work is financially supported by the Science and Engineering Research Board (SERB) under Research Grant (No. ECR/2017/000845), Department of Science and Technology (DST)-Ramanujan Research Grant (No. SB/S2/RJN-081/2016) and Nanomission Research Grant [SR/NM/NS-1036/2017(G)] of the Government of India.

[1] S. Mühlbauer, B. Binz, F. Jonietz, C. Pfleiderer, A. Rosch, A. Neubauer, R. Georgii, and P. Böni, Skyrmion lattice in a chiral magnet, Science **323**, 915 (2009).

[2] C. Pfleiderer, T. Adams, A. Bauer, W. Biberacher, B. Binz, F. Birkelbach, P. Boni, C. Franz, R. Georgii, and M. Janoschek, Skyrmion lattices in metallic and semiconducting B20 transition metal compounds, J.Phys.: Condens. Matter **22**, 164207 (2010).

[3] X. Z. Yu, Y. Onose, N. Kanazawa, J. H. Park, J. H. Han, Y. Matsui1, N. Nagaosa, and Y. Tokura, Real-space observation of a two-dimensional skyrmion crystal, Nature **465**, 901 (2010).

[4] X. Z. Yu, N. Kanazawa, Y. Onose, K. Kimoto, W. Z. Zhang, Y. Matsui, and Y. Tokura, Near room-temperature formation of a skyrmion crystal in thin-films of the helimagnet FeGe, Nat. Mater. **10**, 106 (2011).

[5] S. Seki, X. Z. Yu, S. Ishiwata, and Y. Tokura, Observation of skyrmions in a multiferroic material, Science **336**, 198 (2012).

[6] K. Shibata, X. Z. Yu, T. Hara, D. Morikawa, N. Kanazawa, K. Kimoto, S. Ishiwata, Y. Matsui, and Y. Tokura, Towards control of the size and helicity of skyrmions in helimagnetic alloys by spin–orbit coupling, Nat. Nanotechnol. **8**, 723 (2013).

[7] T. Tanigaki, K. Shibata, N. Kanazawa, X. Yu, Y. Onose, H. S. Park, D. Shindo, and Y. Tokura, Real-space observation of short-period cubic lattice of skyrmions in MnGe, Nano Lett. **15**, 5438 (2015).

[8] Y. Tokunaga, X. Z. Yu, J. S. White, H. M. Rønnow, D. Morikawa, Y. Taguchi, and Y. Tokura, A new class of chiral materials hosting magnetic skyrmions beyond room temperature, Nat. Commun. **6**, 7638 (2015).

[9] I. Kezsmarki, S. Bordacs, P. Milde, E. Neuber, L. Eng, J. White, H. M. Rønnow, C. Dewhurst, M. Mochizuki, and K. Yanai *et al.*, Néel-type skyrmion lattice with confined orientation in the polar magnetic semiconductor GaV_4S_8, Nat. Mater. **14**, 1116 (2015).

[10] A. O. Leonov and I. Kézsmárki, Skyrmion robustness in noncentrosymmetric magnets with axial symmetry: The role of anisotropy and tilted magnetic fields, Phys. Rev. B **96**, 214413 (2017).

[11] B. Gross, S. Philipp, K. Geirhos, A. Mehlin, S. Bordács, V. Tsurkan, A. Leonov, I. Kézsmárki, and M. Poggio, Stability of Néel-type skyrmion lattice against oblique magnetic fields in GaV_4S_8 and GaV_4Se_8, Phys. Rev. B **102**, 104407 (2020).

[12] Korbinian Geirhos, Boris Gross, Bertalan G. Szigeti, Andrea Mehlin, Simon Philipp, Jonathan S. White, Robert Cubitt, Sebastian Widmann, Somnath Ghara, Peter Lunkenheimer, Vladimir Tsurkan, Erik Neuber, Dmytro Ivaneyko, Peter Milde, Lukas M. Eng, Andrey O. Leonov, Sándor Bordács, Martino Poggio, and I. Kézsmárki, Macroscopic manifestation of domain-wall magnetism and magnetoelectric effect in a Néel-type skyrmion host, Npj Quantum Mater. **5**, 44 (2020).

[13] A. K. Nayak, V. Kumar, T. Ma, P. Werner, E. Pippel, R. Sahoo, F. Damay, U. K. Rößler, C. Felser, and S. S. P. Parkin, Magnetic antiskyrmions above room temperature in tetragonal Heusler materials, Nature **548**, 561 (2017).

[14] R. Saha, A. K. Srivastava, T. Ma, J. Jena, P. Werner, V. Kumar, C. Felser, and S. S. P. Parkin, Intrinsic stability of magnetic anti-skyrmions in the tetragonal inverse Heusler compound $Mn_{1.4}Pt_{0.9}Pd_{0.1}Sn$, Nat. Commun. **10**, 5305 (2019).

[15] Sk. Jamaluddin, S. K. Manna, B. Giri, P. V. P. Madduri, S. S. P. Parkin, and A. K Nayak, Robust antiskyrmion phase in bulk tetragonal Mn–Pt(Pd)–Sn Heusler system probed by magnetic entropy change and AC-susceptibility measurements, Adv. Func. Mater. **29**, 1901776 (2019).

[16] L. Peng, R. Takagi, W. Koshibae, K. Shibata, K. Nakajima, T.-h. Arima, N. Nagaosa, S. Seki, X. Yu, and Y. Tokura, Controlled transformation of skyrmions and antiskyrmions in a non-centrosymmetric magnet, Nat. Nanotechnol. **15**, 181 (2020).

[17] J. Jena, B. Göbel, T. Ma, V. Kumar, R. Saha, I. Mertig, C. Felser, and S. S. P. Parkin, Elliptical Bloch skyrmion chiral twins in an antiskyrmion system, Nat. Commun. **11**, 1115 (2020).

[18] P. V. P. Madduri, S. Sen, B. Giri, D. Chakrabartty, S. K. Manna, S. S. P. Parkin, and A. K. Nayak, ac susceptibility study of magnetic relaxation phenomena in the antiskyrmion-hosting tetragonal Mn-Pt(Pd)-Sn system, Phys. Rev. B **102**, 174402 (2020).

[19] T. Schulz, R. Ritz, A. Bauer, M. Halder, M. Wagner, C. Franz, C. Pfleiderer, K. Everschor, M. Garst, and A. Rosch, Emergent electrodynamics of skyrmions in a chiral magnet, Nat. Phys. **8**, 301 (2012).

[20] N. Nagaosa and Y. Tokura, Topological properties and dynamics of magnetic skyrmions, Nat. Nanotech. **8**, 899 (2013).

[21] S. Huang, C. Zhou, G. Chen, H. Shen, A. K. Schmid, K. Liu, and Y. Wu, Stabilization and current-induced motion of antiskyrmion in the presence of anisotropic Dzyaloshinskii-Moriya interaction, Phys. Rev. B **96**, 144412 (2017).

[22] S. Sen, C. Singh, P. K. Mukharjee, R. Nath, and A. K. Nayak, Observation of the topological Hall effect and signature of room-temperature antiskyrmions in Mn-Ni-Ga D_2d Heusler magnets, Phys. Rev. B **99**, 134404 (2019).

[23] See Supplemental Material at http://link.aps.org/supplemental/10.1103/PhysRevApplied.17.044040 for sample characterization, and magnetic and transport measurements.

[24] T. Graf, C. Felser, and S. S. P. Parkin, Simple rules for the understanding of Heusler compounds, Prog. Solid State Chem. **39**, 1 (2011).

[25] N. Nagaosa, J. Sinova, S. Onoda, A. H. MacDonald, and N. P. Ong, Anomalous Hall effect, Rev. Mod. Phys. **82**, 1539 (2010).

[26] A. Bauer and C. Pfleiderer, Magnetic phase diagram of MnSi inferred from magnetization and ac susceptibility, Phys. Rev. B **85**, 214418 (2012).

[27] F. Qian, H. Wilhelm, A. Aqeel, T. T. M. Palstra, A. J. E. Lefering, E. H. Brück, and C. Pappas, Phase diagram and magnetic relaxation phenomena in Cu_2OSeO_3, Phys. Rev. B **94**, 064418 (2016).

[28] Á. Butykai, S. Bordács, L. F. Kiss, B. György Szigeti, V. Tsurkan, A. Loidl, and I. Kézsmárki1, Relaxation dynamics of modulated magnetic phases in the skyrmion host GaV_4S_8 : An ac magnetic susceptibility study, Phys. Rev. B **96**, 104430 (2017).

[29] L. J. Bannenberg, F. Weber, A. J. E. Lefering, T. Wolf, and C. Pappas, Magnetization and ac susceptibility study of the cubic chiral magnet $Mn_{1-x}Fe_xSi$, Phys. Rev. B **98**, 184430 (2018).

[30] K. Karube, J. S. White, D. Morikawa, C. D. Dewhurst, R. Cubitt, A. Kikkawa, X. Yu, Y. Tokunaga, T.-h. Arima, H. M. Rønnow, Y. Tokura, and Y. Taguchi, Disordered skyrmion phase stabilized by magnetic frustration in a chiral magnet, Sci. Adv. **4**, eaar7043 (2018).

[31] X. S. Wang, H. Y. Yuan, and X. R. Wang, A theory on skyrmion size, Commun Phys **1**, 31 (2018).

[32] S. V. Andreev, M. I. Bartashevich, V. I. Pushkarskya, V. N. Maltsev, L. A. Pamyatnykh, E. N. Tarasov, N. V. Kudrevatykh, and T. Goto, Law of approach to saturation in highly anisotropic ferromagnets application to Nd-Fe-B melt-spun ribbons, J. Alloys Compd. **260**, 196 (1997).

[33] M. Sato and Y. Ishii, Simple and approximate expressions of demagnetizing factors of uniformly magnetized rectangular rod and cylinder, J. Appl. Phys. **66**, 983 (1989).

[34] Amikam Aharonia, Demagnetizing factors for rectangular ferromagnetic prisms, J. Appl. Phys. **83**, 6 (1998).

[35] R. Prozorov and V. G. Kogan, Effective Demagnetizing Factors of Diamagnetic Samples of Various Shapes, Phys. Rev. Appl. **10**, 014030 (2018).

[36] A. Neubauer, C. Pfleiderer, B. Binz, A. Rosch, R. Ritz, P. G. Niklowitz, and P. Boni, Topological Hall Effect in the *A* Phase of MnSi, Phys. Rev. Lett. **102**, 186602 (2009).
[37] M. J. Donahue and D. G Porter, OOMMF User's Guide, Version 1.0, Interagency Report NISTIR (2009).
[38] S. Rohart and A. Thiaville, DMExchange6Ngbr, http://math.nist.gov/oommf/contrib/oxsext (2012).
[39] S. Heinze, K. von Bergmann, M. Menzel, J. Brede, A. Kubetzka, R. Wiesendanger, G. Bihlmayer, and S. Blügel, Spontaneous atomic-scale magnetic skyrmion lattice in two dimensions, Nat. Phys. **7**, 713 (2011).
[40] N. Romming, C. Hanneken, M. Menzel, J. E. Bickel, B. Wolter, K. von Bergmann, A. Kubetzka, and R. Wiesendanger, Writing and deleting single magnetic skyrmions, Science **341**, 636 (2013).
[41] T. Kurumaji, T. Nakajima, M. Hirschberger, A. Kikkawa, Y. Yamasaki, H. Sagayama, H. Nakao, Y. Taguchi, T.-H. Arima, and Y. Tokura, Skyrmion lattice with a giant topological Hall effect in a frustrated triangular-lattice magnet, Science **365**, 914 (2019).
[42] M. Hirschberger, T. Nakajima, S. Gao, L. Peng, A. Kikkawa, T. Kurumaji, M. Kriener, Y. Yamasaki, H. Sagayama, H. Nakao, K. Ohishi, K. Kakurai, Y. Taguchi, X. Yu, T. Arima, and Y. Tokura, Skyrmion phase and competing magnetic orders on a breathing kagomé lattice, Nat. Commun. **10**, 5831 (2019).
[43] N. D. Khanh, T. Nakajima, X. Yu, S. Gao, K. Shibata, M. Hirschberger, Y. Yamasaki, H. Sagayama, H. Nakao, L. Peng, K. Nakajima, R. Takagi, T.-h. Arima, Y. Tokura, and S. Seki, Nanometric square skyrmion lattice in a centrosymmetric tetragonal magnet, Nat. Nanotechnol. **15**, 444 (2020).
[44] J. Tang, Y. Wu, W. Wang, L. Kong, B. Lv, W. Wei, J. Zang, M. Tian, and H Du, Magnetic skyrmion bundles and their current-driven dynamics, Nat. Nanotechnol. **16**, 1086 (2021).